

ARTICLE OPEN



Probing resonating valence bonds on a programmable germanium quantum simulator

Chien-An Wang^{1,3}, Corentin Déprez^{1,3}, Hanifa Tidjani¹, William I. L. Lawrie¹, Nico W. Hendrickx¹, Amir Sammak², Giordano Scappucci¹ and Menno Veldhorst¹✉

Simulations using highly tunable quantum systems may enable investigations of condensed matter systems beyond the capabilities of classical computers. Quantum dots and donors in semiconductor technology define a natural approach to implement quantum simulation. Several material platforms have been used to study interacting charge states, while gallium arsenide has also been used to investigate spin evolution. However, decoherence remains a key challenge in simulating coherent quantum dynamics. Here, we introduce quantum simulation using hole spins in germanium quantum dots. We demonstrate extensive and coherent control enabling the tuning of multi-spin states in isolated, paired, and fully coupled quantum dots. We then focus on the simulation of resonating valence bonds and measure the evolution between singlet product states which remains coherent over many periods. Finally, we realize four-spin states with *s*-wave and *d*-wave symmetry. These results provide means to perform non-trivial and coherent simulations of correlated electron systems.

npj Quantum Information (2023)9:58; <https://doi.org/10.1038/s41534-023-00727-3>

INTRODUCTION

Quantum computers have the potential of simulating physics beyond the capacity of classical computers^{1–4}. Gate-defined quantum dots are extensively studied for quantum computation^{5,6}, but are also a natural platform for implementing quantum simulations^{7–11}. The control over the electrical charge degree of freedom has facilitated the exploration of novel configurations such as effective attractive electron–electron interactions¹², collective Coulomb blockade¹³ and topological states¹⁴. Coherent systems may be simulated when using the spin states of electrons in quantum dots, though experiments thus far have relied on gallium arsenide heterostructures^{15–17}, where the hyperfine interaction limits the spin coherence and therefore the complexity of simulations that can be performed. This bottleneck can be tackled by using group IV materials with nuclear spin-free isotopes. A natural candidate would be silicon, but this material comes with additional challenges due to the presence of valley states and a large effective electron mass¹⁸.

Hole quantum dots in planar Ge/SiGe heterostructures exhibit many favorable properties found in different quantum dot platforms¹⁹. Natural germanium has a high abundance of nuclear spin-free isotopes and can be isotopically purified²⁰. Holes in germanium benefit from a low effective mass^{21,22}, absence of valley degeneracies, ohmic contacts to metals²³, and strong spin-orbit coupling for all-electrical control^{24,25}. Recent advances in heterostructure growth have resulted in stable, low-noise germanium devices²⁶. This has sparked rapid progress, with demonstrations of hole quantum dots²³, single hole qubits²⁵, singlet-triplet (ST) qubits²⁷, two-qubit logic²⁸ and a four qubit quantum processor²⁹.

Here, we explore the prospects of hole quantum dots in Ge/SiGe for quantum simulation. We focus on the simulation of resonating valence bond (RVB) states, which are of fundamental relevance in chemistry³⁰ and solid state physics^{31–34} and have been used in other platforms as a feasibility test for quantum

simulation^{35–38}. In our simulation, we probe RVB states in a square 2×2 configuration. First, we realize ST qubits for all nearest-neighbor configurations. We then study the coherent evolution of four-spin states and demonstrate exchange control spanning an order of magnitude. Furthermore, we tune the system to probe valence bond resonances whose observed characteristics comply with predictions derived from the Heisenberg model. We finally demonstrate the preparation of *s*-wave and *d*-wave RVB states from spin-singlet states via adiabatic initialization and tailored pulse sequences.

RESULTS

RVB simulation in a quantum dot array with a square geometry

The experiments are based on a quantum dot array defined in a high-quality Ge/SiGe quantum well, as shown in Fig. 1a^{29,39}. The array comprises four quantum dots and we obtain good control over the system, enabling to confine zero, one, or two holes in each quantum dot as required for the quantum simulation. The dynamics of resonating valence bonds is governed by Heisenberg interactions. The spin states in germanium quantum dots, however, also experience Zeeman, spin-orbit and hyperfine interactions (see Supplementary Note 6). We therefore operate in small magnetic fields and acquire a detailed understanding of the system dynamics to apply tailored pulses. In the regime where Heisenberg interactions are dominating, the total spin is conserved. We can therefore study the subspaces of different total spin separately. The relevant subspace for the RVB physics is the zero total spin space spanned by the basis formed by the four-spin states $|S_x\rangle = |S_{12}S_{34}\rangle$ and $\frac{1}{\sqrt{3}}(|T_{12}^+T_{34}^- \rangle + |T_{12}^-T_{34}^+ \rangle - |T_{12}^0T_{34}^0 \rangle)$, where $|S_{ij}\rangle = \frac{1}{\sqrt{2}}(|\uparrow_i\downarrow_j\rangle - |\downarrow_i\uparrow_j\rangle)$ and $|T_{ij}^0\rangle = \frac{1}{\sqrt{2}}(|\uparrow_i\downarrow_j\rangle + |\downarrow_i\uparrow_j\rangle)$, $|T_{ij}^+\rangle = |\uparrow_i\uparrow_j\rangle$, $|T_{ij}^-\rangle = |\downarrow_i\downarrow_j\rangle$ denote the singlet and triplet states formed by the spins in the quantum dots *i* and *j*. In this basis, the

¹QuTech and Kavli Institute of Nanoscience, Delft University of Technology, PO Box 5046, 2600 GA Delft, The Netherlands. ²QuTech and Netherlands Organisation for Applied Scientific Research (TNO), Delft, The Netherlands. ³These authors contributed equally: Chien-An Wang, Corentin Déprez. ✉email: M.Veldhorst@tudelft.nl

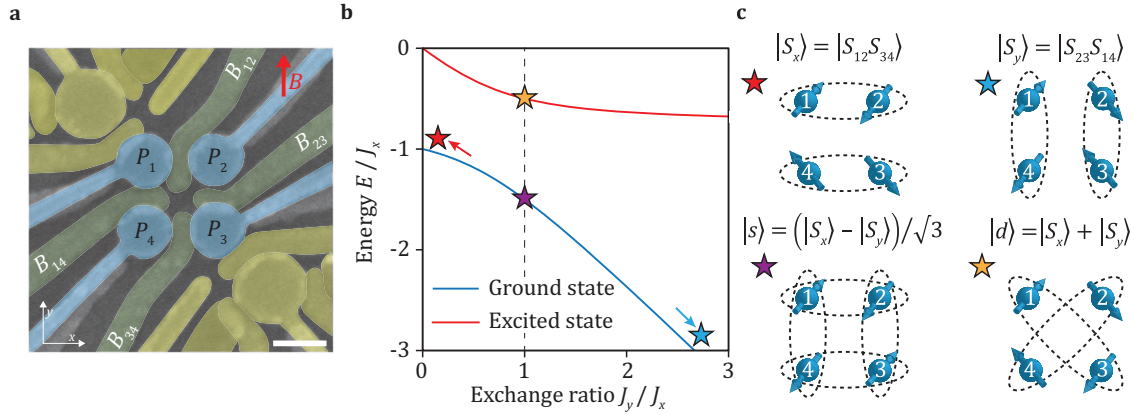


Fig. 1 RVB states in a 2×2 quantum dot array. **a** False-colored scanning electron micrograph of the Ge quantum dot array. Plunger and barrier gates are colored in blue and green respectively, and the corresponding gate voltages applied on them are labeled. To achieve independent control of the quantum dot potentials and tunnel couplings, virtual plunger and barrier gate voltages are defined (see Supplementary Note 1). Single hole transistors used as charge sensors are colored in yellow. The scale bar corresponds to 100 nm. **b** Energy diagram corresponding to the Hamiltonian H_S . The stars denote the corresponding eigenstates depicted in **(c)**. When the exchange interaction is dominated by horizontal (vertical) pairs, the ground state is $|S_x\rangle$ ($|S_y\rangle$), and in our experiments we use this configuration for initialization. Resonating valence bond states appear when $J_y = J_x$, the eigenstates are the ground state with s -wave symmetry and excited state with d -wave symmetry.

Heisenberg Hamiltonian H_J reads:

$$H_J(S_{\text{tot}} = 0) \equiv H_S = \begin{pmatrix} -J_x - \frac{J_y}{4} & \frac{\sqrt{3}}{4} J_y \\ \frac{\sqrt{3}}{4} J_y & -\frac{3}{4} J_y \end{pmatrix}, \quad (1)$$

where $J_x = J_{12} + J_{34}$ and $J_y = J_{14} + J_{23}$. Figure 1b, c shows the eigen energies and eigenstates of H_S for different regimes of exchange interaction. When the exchange interaction is turned on in only one direction, $J_x \gg J_y$ or $J_x \ll J_y$, the system is equivalent to two uncoupled double quantum dots. The ground state is then a product of singlet states $|S_x\rangle$ or $|S_y\rangle = |S_{14}S_{23}\rangle$. However, when all exchanges are on and in particular when they are equal, $J_x = J_y$, the eigenstates are coherent superpositions of $|S_x\rangle$ and $|S_y\rangle$, which simulate the RVB state. In this regime, the ground state is the s -wave superposition state $|s\rangle = \frac{1}{\sqrt{3}}(|S_x\rangle - |S_y\rangle)$ and the excited state is the d -wave superposition state $|d\rangle = |S_x\rangle + |S_y\rangle$.

Figure 1b shows that RVB states can be generated from uncoupled spin singlets by adiabatically equalizing the exchange couplings. Alternatively, if the exchange couplings are pulsed diabatically to equal values, valence bond resonances between $|S_x\rangle$ and $|S_y\rangle$ states occur.

Singlet-Triplet oscillations in the four double quantum dots

Probing the RVB physics relies on measuring the singlet probabilities in the (1,1) charge state^{17,36}. We thus investigate ST oscillations within all nearest-neighbor pairs.

To generate ST oscillations, we operate in a virtual gate landscape and apply pulses on the virtual plunger gates vP_i of each quantum dot pair according to the pulse sequence depicted in Fig. 2a^{27,40–43}. The double quantum dot system is initialized in a singlet (0,2) state. Then, the detuning between the quantum dots is varied by changing the virtual plunger gate voltages. The system is diabatically brought to a manipulation point in the (1,1) sector creating a coherent superposition of $|S\rangle$, $|T^-\rangle$ and $|T^0\rangle$ ^{27,40–43}. After a dwell time t_D , the system is diabatically pulsed back to the (0,2) sector where the ST probabilities are determined via single-shot readout using (latched) Pauli-spin-blockade^{44–46}.

Results of such experiments performed at $B = 3$ mT with Q_3Q_4 pair are presented in Fig. 2c. Clear oscillations between the $|S\rangle$ and $|T^-\rangle$ state are observed over a large range of gate voltage. Importantly, using this method we find the S - T^- anticrossing, which is the position where the frequency has a minimum. The

observation of such oscillations, predominating over oscillations between $|S\rangle$ and $|T^0\rangle$ states, agrees with recent investigations suggesting that S - T^- oscillations dominate in germanium ST qubits placed in an in-plane B field⁴³.

Figure 2c also suggests that a (1,1)-singlet can be initialized from a (0,2)-singlet, by changing the energy detuning between the quantum dots while avoiding to pass the S - T^- anticrossing. We achieve this by shifting the anticrossing towards the center of the (1,1) charge sector by decreasing the magnetic field to $B = 1$ mT and increasing the tunnel couplings (Supplementary Fig. 1). Figure 2d demonstrates clear S - T^- oscillations observed in this regime for all nearest-neighbor configurations (see also Supplementary Fig. 2). Importantly, these oscillations also enable to determine the singlet/triplet states on two parallel quantum dot pairs by using sequential readout⁴⁷.

Tuning of individual exchanges using coherent oscillations

The overlap of the H_S eigenstates with $|S_x\rangle$ and $|S_y\rangle$ depends on J_x and J_y (see Supplementary Note 4). A quantitative comparison between experiments and theoretical expectations thus requires fine control over the exchange couplings.

In this purpose, we focus on the evolution of coherent four-spin ST oscillations. These oscillations are induced using the experimental sequence depicted in Fig. 3a (see also Supplementary Fig. 3). We turn off two parallel exchange couplings and initialize a $|S_x\rangle$ or a $|S_y\rangle$ state in parallel double quantum dots. We then rotate one of the singlet pairs to a triplet $|T^-\rangle$ state through coherent time evolution after pulsing to the S - T^- anticrossing, creating a four-spin singlet-triplet product state (e.g., $|T_{34}S_{12}\rangle$ or $|T_{23}S_{14}\rangle$). All barrier gate voltages are then diabatically pulsed to turn on all the exchange couplings leading to coherent evolution of the four-spin system. After a dwell time t_D , two pairs are isolated (not necessarily the initial ones) and their spin-states are readout sequentially, which allows to deduce spin-correlations of opposite pairs, as was realized in linear arrays in GaAs¹⁷.

The observation of resonating valence bond requires equal couplings between all four quantum dots. In navigating to this point, we carefully develop a virtual landscape, keep control over all the individual exchange interactions. First, we separately equalize the horizontal ($J_{12} = J_{34}$) and vertical ($J_{14} = J_{23}$) exchange couplings. Then, we tune the vertical and horizontal exchanges to the same coupling strength. The Chevron patterns displayed in

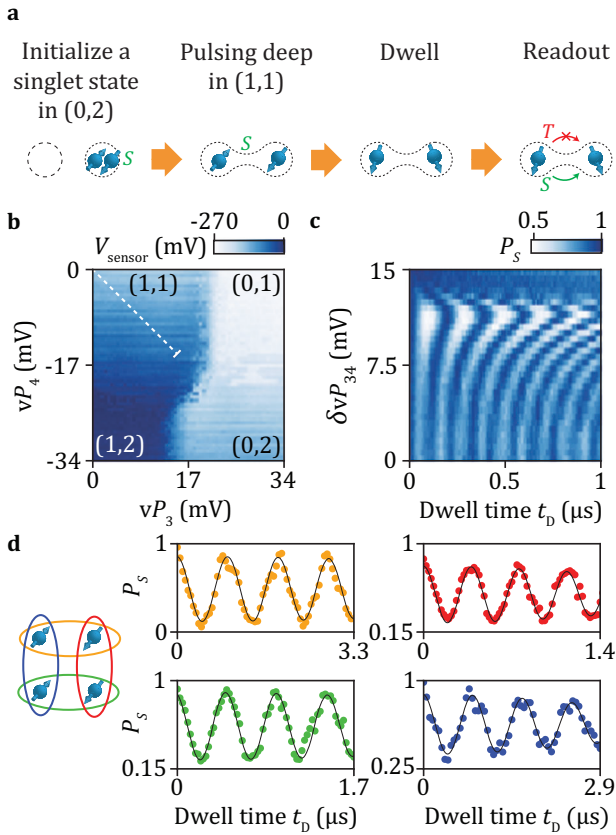


Fig. 2 Singlet-triplet qubits on all nearest-neighbor configurations. **a** Schematics of the pulse sequence used to generate singlet-triplet oscillations in double quantum dots. **b** Charge stability diagram of a double quantum dot (Q_3Q_4) in the few-hole regime. **c** S^-T^- oscillations as a function of time and detuning $\delta v P_{34} = 0.5(v P_3 - v P_4)$ varied along the dashed line in **(b)**. At larger magnetic fields, here $B = 3$ mT, and limited tunnel couplings, we observe a minimum oscillation frequency due to the S^-T^- anticrossing. We tune the system in a regime with smaller magnetic fields ($B = 1$ mT) and larger tunnel couplings, to operate away from this point. **d** S^-T^- oscillations observed in this regime for all possible permutations of nearest-neighbor quantum dot pairs. Black lines are fits to the data (see Supplementary Note 2).

Fig. 3c, d are consistent with a Heisenberg Hamiltonian (see Supplementary Figs. 4–6) and the minima in the oscillation frequency mark the location of equal exchange couplings for horizontal ($J_{12} \approx J_{34} \approx J_x/2$ for Fig. 3c) or vertical pairs ($J_{14} \approx J_{23} \approx J_y/2$ for Fig. 3d). Through an iterative process, we can find ranges of virtual gate voltages where $J_{12} \approx J_{34}$ and $J_{23} \approx J_{14}$.

We can now control the spin pairs simultaneously, while maintaining the exchange couplings in both the horizontal and vertical directions equal (see Supplementary Note 5), with a priori $J_x \neq J_y$. Through the readout of both pairs, we can obtain the frequency of four-spin ST oscillations observed in this regime (Fig. 3e), which is given by $f_{ST} = J_y/2h$ or $J_x/2h$ depending on the initial state, and with that determine the exchange interaction. As highlighted in Fig. 3f, the virtual control enables to tune J_x from 15 MHz to 109 MHz with J_y remaining between 46 and 56 MHz. Clearly, the exchange interaction can be controlled and measured over a significant range and tuned to a regime where all couplings are equal (we obtain a precision of ≈ 3 MHz, as discussed in Supplementary Note 5, mostly determined by drifts between experiments).

Valence bond resonances

Valence band resonances can occur when all J_{ij} are equal. To experimentally assess this, we prepare $|S_x\rangle$ or $|S_y\rangle$, which are superposition states of H_S . We then pulse the exchanges such that $J_x \approx J_y$. Figure 4a shows the result of the time evolution in this regime of equal exchange couplings. Since we start from a superposition state of H_S , the time evolution leads to coherent oscillations between $|S_x\rangle$ and $|S_y\rangle$, which results in periodic swaps between the singlet states as depicted in Fig. 4b. In addition, we readout both in the horizontal and vertical configuration, and observe an anti-correlated signal, consistent with signatures of valence bond resonances^{32,36}. The observation of more than ten oscillations shows the relatively high level of coherence achieved during these experiments further confirmed by the characteristic dephasing time $T_\phi \approx 150$ ns.

Figure 4c, d shows a more detailed measurement, which we can fit using $\frac{\mathcal{V}_{xy}}{2} \cos(2\pi f_{SS} t_D + \phi) \exp(-t_D/T_\phi)^2 + A_0$ to extract the evolution of the frequencies f_{SS} and of the visibilities $\mathcal{V}_{x,y}$, plotted on Fig. 4e and Fig. 4f. We find a quantitative agreement between the measured frequencies and the theoretical expectation $f_{SS} =$

$\sqrt{J_x^2 + J_y^2 - J_x J_y}/h$ despite deviations for the lowest values of $\delta V'_x$ that could result from the uncertainties in the exchange couplings. We also find a qualitative agreement for the visibilities though the measured $\mathcal{V}_{x,y}$ remain lower, in particular when the exchange is larger. Fermi-Hubbard simulations and further analysis (see Supplementary Notes 7 and 8) reveal that part of the visibility loss can be attributed to leakage and to the insufficient diabaticity of the voltages pulses. We speculate that the rest of the visibility loss is mainly due to the decoherence induced by the voltage pulses at the manipulation stage, or by pulse distortion arising from the non-ideal electrical response of the wiring. The underlying mechanism affects similarly the results of the measurements in the both readout directions over most of the voltage range spanned (see Supplementary Note 8). Consequently, a more quantitative agreement is reached when comparing the ratio $\mathcal{V}_y/(\mathcal{V}_x + \mathcal{V}_y)$ (Fig. 4g) of the visibilities measured over the visibilities predicted, similarly as is done in ref.³⁶. Overall, the good agreement observed confirms that the dynamics is governed by H_S .

Preparation of resonating valence bond eigenstates

Having observed valence bond resonances, we now focus on the preparation of eigenstates of H_S which are the $|s\rangle$ and $|d\rangle$ RVB states. $|s\rangle$ is the ground state of H_S when $J_x = J_y$, whereas $|S_x\rangle$ and $|S_y\rangle$ are the ground states when $J_x \gg J_y$ and $J_x \ll J_y$. Experimentally we therefore prepare $|s\rangle$ from $|S_x\rangle$ or $|S_y\rangle$ by adiabatically tuning the exchange interactions to equal values. Figure 5a shows experiments where we control the ramp time t_{ramp} to tune to this regime and we observe a progressive vanishing of phase oscillations. For large $t_{\text{ramp}} \gtrsim 140$ ns, the oscillations nearly disappear and the measured probability saturates to $P_{S_{12}S_{34}} \approx 0.78$. Performing similar experiments starting from a $|S_y\rangle$ state or measuring $P_{S_{23}S_{14}}$ leads to identical features with singlet-singlet probabilities saturating between 0.66 and 0.72 (see Supplementary Fig. 22). These values are close to the probabilities $|\langle S_{x,y}|s\rangle|^2 = 3/4$ expected when the s -wave state is prepared.

We can now also prepare the ground state H_S for arbitrary exchange values, by carefully tuning the ramp time ($t_{\text{ramp}} = 160$ ns in our experiments). Figure 5b shows the evolution of $P_{S_{12}S_{34}}$ for different $\delta V'_x$. Since we prepare the ground state, coherent phase evolution results in a $P_{S_{12}S_{34}}$ that is virtually constant for any $\delta V'_x$ and only faint oscillations are observed. $P_{S_{12}S_{34}}$, however, is strongly dependent on $\delta V'_x$, as increasing J_x changes the ground state to $|S_x\rangle$.

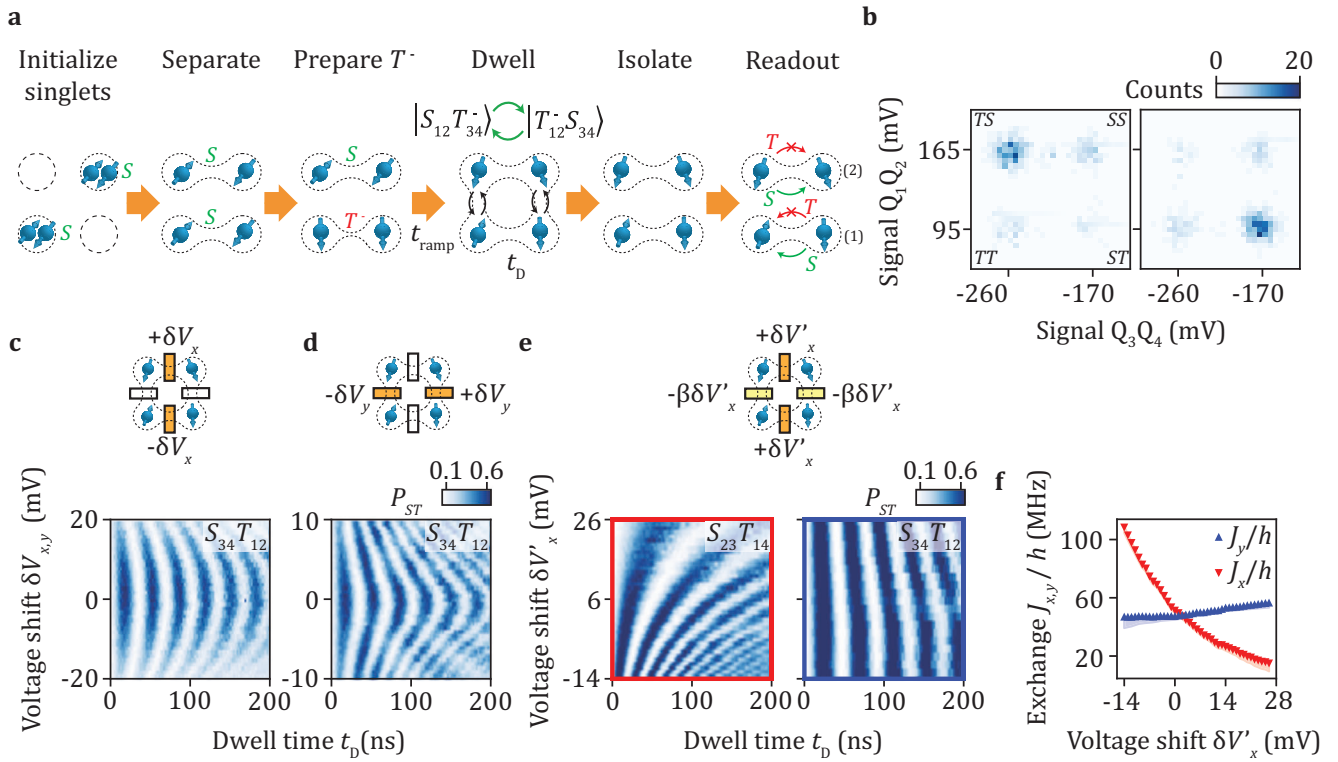


Fig. 3 Four-spin coherent singlet-triplet oscillations and exchange characterization. **a** Schematics of the pulse sequence used to measure four-spin ST oscillations from an initial $|T_{34}^- S_{12}\rangle$ state. **b** The 2D histograms of the sensor signals formed by sequential 500 single-shot readouts of Q_3Q_4 and Q_1Q_2 ST states. The left panel shows the initial state $|T_{34}^- S_{12}\rangle$ at $t_D = 0$ ns. The right panel shows the state at $t_D = 19$ ns corresponding to half an oscillation period. (Data corresponds to (c) for $\delta V_x = 0$). **c** Oscillations in ST probability $P_{S_{34}T_{12}}$ as a function of gate voltage variation δV_x . The amplitude of exchange pulses applied on the virtual barrier gates during the free evolution step are varied between measurements around a predetermined set of barrier gate voltages where $J_x < J_y$. The amplitude of voltage pulses on $vB_{12,34}$ are varied anti-symmetrically while the amplitudes of the pulses on $vB_{23,14}$ are kept constant, as shown in the top illustration. The initial state is $|T_{34}^- S_{12}\rangle$. **d** Similar experiment where oscillations in $P_{S_{34}T_{12}}$ are studied as a function of the gate voltage variation δV_y . δV_y is the shift in the amplitudes of the exchange pulses applied anti-symmetrically on $vB_{23,14}$ (see top illustration). The initial state is $|T_{34}^- S_{12}\rangle$. **e** Oscillations in $P_{S_{23}T_{14}}$ (left) and $P_{S_{34}T_{12}}$ (right) as functions of t_D and $\delta V'_x$. The amplitude of exchange pulses are varied symmetrically around the operation point ($\delta V'_x = 0$ mV where $J_x \approx J_y$) according to the top illustration ensuring that $J_{12} \approx J_{34}$ and $J_{14} \approx J_{23}$ along the full voltage range. The initial states are respectively a $|T_{23}^- S_{14}\rangle$ (left) and a $|T_{34}^- S_{12}\rangle$ state (right). **f** Exchange couplings $J_{x,y}$ extracted by fitting the oscillations in (e) with $A \cos(2\pi f_{ST} t_D + \phi) \exp(-(t_D/T_\phi)^2) + A_0$ as a function of gate voltage variation $\delta V'_x$. The oscillation frequencies of $P_{S_{23}T_{14}}$ ($P_{S_{34}T_{12}}$) corresponds to $J_x/2h$ ($J_y/2h$). The shaded areas correspond to the estimated uncertainty on the exchange couplings derived based on assumptions discussed in Supplementary Note 5.

The measured $P_{S_{12}S_{34}}$ values can be compared with predictions using $J_{x,y}$ values extracted from four-spin singlet-triplet oscillations (see Supplementary Note 4). Figure 5c shows that a good agreement exists between the theory and the experiments. The raw experimental probabilities $P_{S_{12}S_{34}}$ remains smaller than the theoretical predictions due to systematic errors during the experiments, which are most likely state initialization and readout errors (see Supplementary Note 8). Rescaling the data by constant factors, that compensate for systematic errors, allows to reach a quantitative agreement, as shown in Fig. 5c. From this we conclude that the ground state of H_S is adiabatically initialized in these experiments.

We prepare the d -wave state by including an additional operation where we exchange two neighboring spins³⁶. This results in a transformation of neighboring spin-spin correlations to diagonal correlations. We experimentally implement this step by adding, before the free evolution step, an exchange pulse of duration t_j during which only one exchange coupling is turned on (see Fig. 5d).

Figure 5e, f shows $P_{S_{12}S_{34}}$ and $P_{S_{23}S_{14}}$ measured as functions of t_D and t_j in experiments where the system is initialized in $|S_x\rangle$ and the exchange J_{23} is pulsed. As a function of the exchange pulse duration, we observe a periodic vanishing of RVB oscillations (linecuts provided in Fig. 5g, h, imperfections in exchange control cause residual oscillations). Due to the exchange pulse, a periodic swapping of neighboring spins occurs, and thus a periodic evolution between neighboring spin-spin correlations and diagonal correlations. Thus the regime where the d -wave eigenstate is prepared is marked by the vanishing of RVB states. The mean of the probabilities, $P_{S_{23}S_{14}} \approx 0.21$ and $P_{S_{12}S_{34}} \approx 0.13$, measured for $t_j = 25$ ns are in the direction of theoretical expectations $|\langle S_{x,y} | d \rangle|^2 = 1/4$.

DISCUSSION

In this work we demonstrated a coherent quantum simulation using germanium quantum dots. Clear evolution of resonating valence bond states appeared after tuning to a regime where all nearest neighbours have equal exchange coupling. We furthermore

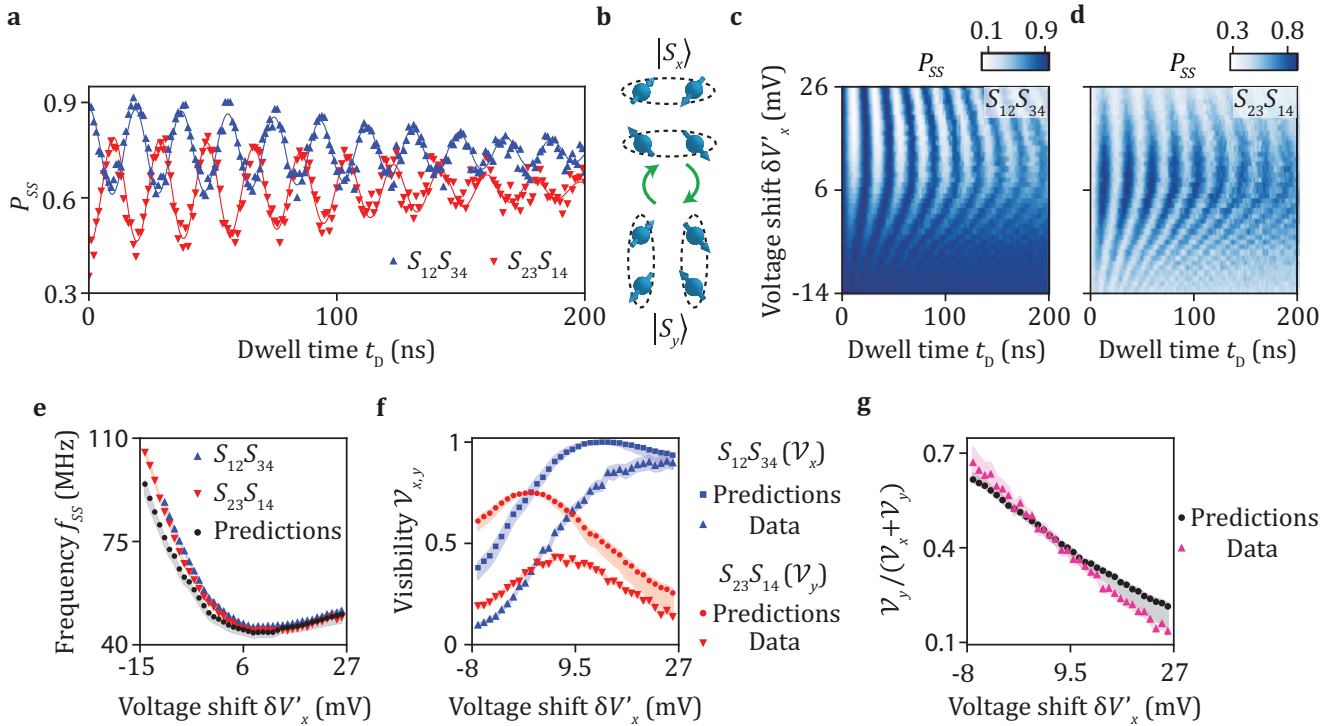


Fig. 4 Valence bond resonances. **a** Probabilities of having horizontal singlet pairs $P_{S_{12}S_{34}}$ and vertical singlet pairs $P_{S_{23}S_{14}}$ as a function of dwell time t_D . All the exchange couplings are tuned toward an identical value of $J_{ij}/h \simeq 25$ MHz. Lines are fits to the data with $P_{SS} = 1/2 \mathcal{V} \cos(2\pi f_{SS} t_D + \phi) \exp(-(t_D/T_\phi)^2) + A_0$ giving respectively $T_\phi = 167$ ns and 143 ns for data corresponding to $P_{S_{12}S_{34}}$ and $P_{S_{23}S_{14}}$. The state is initialized as $|S_x\rangle$. **b** Illustration showing valence bond resonances characterized by oscillations between the singlet product states $|S_x\rangle$ and $|S_y\rangle$. **c** $P_{S_{12}S_{34}}$ and **d** $P_{S_{23}S_{14}}$ as a function of t_D and virtual barrier gate voltage variation $\delta V'_x$. The state is initialized as $|S_x\rangle$. **e** The oscillation frequency f_{SS} as a function of $\delta V'_x$. The blue (red) points are extracted from (c, d). The black points are the theoretical predictions $f_{SS} = \sqrt{J_x^2 + J_y^2 - J_x J_y}/h$ computed using the exchanges J_x and J_y measured in Fig. 3e. **f** Visibility $\mathcal{V}_{x,y}$ as a function of gate voltage variation $\delta V'_x$. The triangles in blue (red) are extracted from (c, d). The shaded areas correspond to one standard deviation from the best fit for the experimental data, and for the theoretical data they correspond to the uncertainties on the amplitude and the frequency computed using the uncertainties on the exchange couplings values. **g** Ratio of the visibilities $\mathcal{V}_y/(\mathcal{V}_x + \mathcal{V}_y)$ as a function of the gate voltage variation $\delta V'_x$.

established the preparation of the *s*-wave and *d*-wave eigenstates. In addition, we have shown that we can control the exchange interaction over a significant range in a multi-spin setting.

The low-disorder and quantum coherence make germanium a compelling candidate for more advanced quantum simulations. Improving the initialization and readout fidelities will enable to observe a stronger correspondence between ideal predictions and experimental results. Additionally, advanced voltage pulsing may facilitate to reduce errors occurring when controlling the spin states. Furthermore, a significant improvement in the quantum coherence may be obtained by exploring sweet spots⁴⁸ and by using purified germanium.

Controlling multi-spin states is also highly relevant in the context of quantum computation. The realization of exchange-coupled singlet-triplet qubits enables to implement fast two-qubit gates^{49–52}. Leakage may then be reduced by exploiting the large out-of-plane *g*-factor for holes in germanium^{27,43}. Also, operation with four-spin manifolds provides means for decoherence-free subspaces⁵³.

Extensions of this work leveraging the full tunability of germanium quantum dots could provide new insights for extensive studies of strongly-correlated magnetic phases and associated quantum phase transitions. In particular, the implementation of similar simulations in triangular lattices offer new

possibilities to investigate the emergence of non-trivial phases arising from frustration^{33,34}. Likewise, the preparation of RVB states and the investigation of their dynamics in larger devices may help to probe their properties experimentally and explore how they relate to superconductivity in doped cuprates³¹.

METHODS

Materials and device fabrication

The device is fabricated on a strained Ge/SiGe heterostructure grown by chemical vapor deposition. Starting from a natural Si wafer, a 1.6 μm thick relaxed Ge layer is grown, followed by a 1 μm reverse graded $\text{Si}_{1-x}\text{Ge}_x$ (x going from 1 to 0.8) layer, a 500 nm relaxed $\text{Si}_{0.2}\text{Ge}_{0.8}$ layer, a 16 nm Ge quantum well under compressive stress, a 55 nm $\text{Si}_{0.2}\text{Ge}_{0.8}$ spacer layer and a < 1 nm thick Si cap. The quantum well is contacted by aluminum ohmic contacts after a buffered oxide etch of the oxidized Si cap. The ohmics are isolated from the gates by a 10 nm ALD grown alumina layer. Two sets of Ti/Pd gates, separated by 7 nm of alumina, are deposited on top of the heterostructure to define the quantum dots. The potential of the quantum dots is tuned using the plunger gates (blue in Fig. 1a) while barrier gates are used to tune the tunnel couplings between the quantum dots (green).

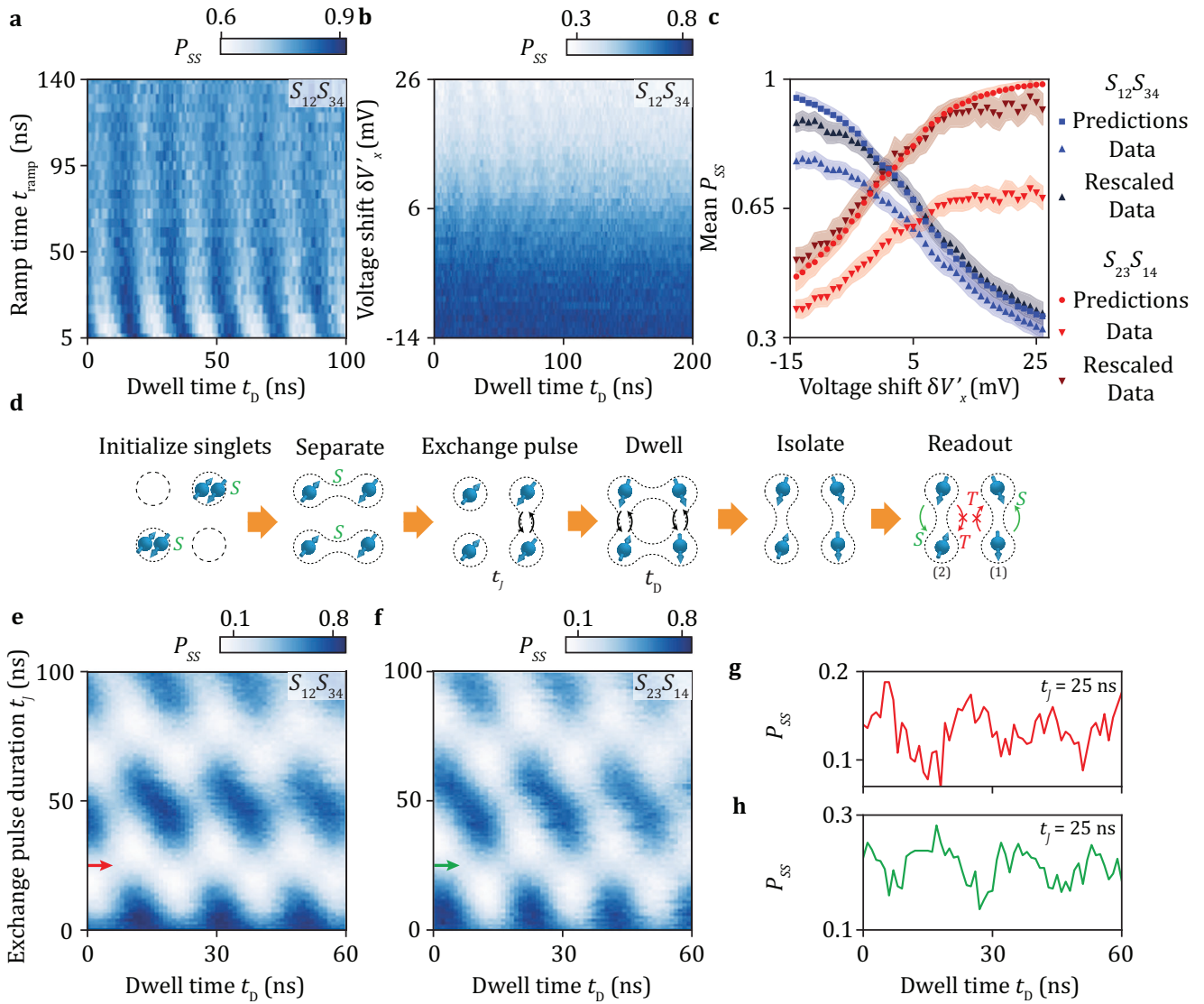


Fig. 5 Initialization of RVB eigenstates. **a** Evolution of RVB oscillations as a function of the time to set all exchanges equal ($J_{ij} \approx 25$ MHz) (see Fig. 3a). For $t_{\text{ramp}} \gtrsim 140$ ns, the ground state with s -wave symmetry is adiabatically prepared. **b** Evolution of the singlet-singlet probability $P_{S_{12}S_{34}}$ with $\delta V'_x$ after adiabatic initialization of the ground state. **c** Evolution of the mean singlet-singlet probability measured after adiabatic initialization of the ground state with $\delta V'_x$ for both readout directions. The experiments are compared to theoretical expectations using exchange coupling values extracted from four-spin singlet-triplet oscillations (Supplementary Notes 4 and 5). The shaded areas correspond to one standard deviation for the experimental data, and for the theoretical data they correspond to the uncertainties on the expected probabilities computed using the uncertainties on the exchange couplings values. Rescaled data (dark red and blue triangles) are obtained by multiplying each raw dataset (red and blue triangles) by a constant factor corresponding to the mean ratio of the predicted probabilities over the measured probabilities. **d** Experimental sequence used to investigate the formation of the d -wave state. Before the free evolution step, one exchange pulse on vB_{23} is applied for a time t_j . **e, f** Evolution of singlet-singlet oscillations measured for different exchange pulse durations t_j . The vanishing of oscillations at $t_j \approx 25$ ns marks the formation of a d -wave state. **g, h** Linecuts of **(e)** and **(f)** for $t_j = 25$ ns.

Experimental set-up

Experiments are performed in the 2×2 array of quantum dots showed in Fig. 1a and the changes of the charge states in the array are measured using two single hole transistors (yellow in Fig. 1a) via rf-reflectometry. Further information regarding the experimental set-up used are provided in ref. ²⁹.

Measurement techniques

Virtual barrier and plunger gate voltages, defined as linear combinations of real gate voltages, are used to tune

independently the potentials/couplings and compensate effects of cross-capacitances (see Supplementary Note 1). For four-spin coherent oscillations, the spin-spin probabilities (or equivalently the spin-spin correlations) are determined by reading out sequentially the states of two parallel quantum dot pairs, either first Q_3Q_4 and then Q_1Q_2 or first Q_2Q_3 and then Q_1Q_4 . While reading one pair, the second is stored deep in the (1,1) charge sector to prevent cross-talk between the measurements^{17,47}. The state of each pairs is determined for each single shot-measurements by comparing the sensor signal to a predetermined threshold.

DATA AVAILABILITY

Data underlying this study are available on a Zenodo repository at <https://zenodo.org/record/7998145>.

Received: 28 October 2022; Accepted: 6 June 2023;

Published online: 17 June 2023

REFERENCES

- Feynman, R. P. Simulating physics with computers. *Int. J. Theor. Phys.* **21**, 467–488 (1982).
- Lloyd, S. Universal quantum simulators. *Science* **273**, 1073–1078 (1996).
- Abrams, D. S. & Lloyd, S. Simulation of many-body Fermi systems on a universal quantum computer. *Phys. Rev. Lett.* **79**, 2586–2589 (1997).
- Aspuru-Guzik, A., Dutoi, A. D., Love, P. J. & Head-Gordon, M. Simulated quantum computation of molecular energies. *Science* **309**, 1704–1707 (2005).
- Loss, D. & DiVincenzo, D. P. Quantum computation with quantum dots. *Phys. Rev. A* **57**, 120–126 (1998).
- Vandersypen, L. M. K. et al. Interfacing spin qubits in quantum dots and donors—hot, dense, and coherent. *npj Quantum Inform.* **3**, 34 (2017).
- Manousakis, E. A quantum-dot array as model for copper-oxide superconductors: a dedicated quantum simulator for the many-fermion problem. *J. Low Temp. Phys.* **126**, 1501–1513 (2002).
- Smirnov, A. Y., Savel'ev, S., Mourokh, L. G. & Nori, F. Modelling chemical reactions using semiconductor quantum dots. *EPL* **80**, 67008 (2007).
- Byrnes, T., Kim, N. Y., Kusudo, K. & Yamamoto, Y. Quantum simulation of Fermi-Hubbard models in semiconductor quantum-dot arrays. *Phys. Rev. B* **78**, 075320 (2008).
- Barthelemy, P. & Vandersypen, L. M. K. Quantum dot systems: a versatile platform for quantum simulations. *Ann. Phys.* **525**, 808–826 (2013).
- Gray, J., Bayat, A., Puddu, R. K., Smith, C. G. & Bose, S. Unravelling quantum dot array simulators via singlet-triplet measurements. *Phys. Rev. B* **94**, 195136 (2016).
- Hamo, A. et al. Electron attraction mediated by Coulomb repulsion. *Nature* **535**, 395–400 (2016).
- Hensgens, T. et al. Quantum simulation of a Fermi-Hubbard model using a semiconductor quantum dot array. *Nature* **548**, 70–73 (2017).
- Kiczynski, M. et al. Engineering topological states in atom-based semiconductor quantum dots. *Nature* **606**, 694–699 (2022).
- Dehollain, J. P. et al. Nagaoka ferromagnetism observed in a quantum dot plaquette. *Nature* **579**, 528–533 (2020).
- Qiao, H. et al. Coherent multispin exchange coupling in a quantum-dot spin chain. *Phys. Rev. X* **10**, 031006 (2020).
- van Diepen, C. J. et al. Quantum simulation of antiferromagnetic Heisenberg chain with gate-defined quantum dots. *Phys. Rev. X* **11**, 041025 (2021).
- Zwanenburg, F. A. et al. Silicon quantum electronics. *Rev. Mod. Phys.* **85**, 961–1019 (2013).
- Scappucci, G. et al. The germanium quantum information route. *Nat. Rev. Mater.* **6**, 926–943 (2021).
- Sigillito, A. J. et al. Electron spin coherence of shallow donors in natural and isotopically enriched germanium. *Phys. Rev. Lett.* **115**, 247601 (2015).
- Sammak, A. et al. Shallow and undoped germanium quantum wells: a playground for spin and hybrid quantum technology. *Adv. Funct. Mater.* **29**, 1807613 (2019).
- Lodari, M. et al. Light effective hole mass in undoped Ge/SiGe quantum wells. *Phys. Rev. B* **100**, 041304 (2019).
- Hendrickx, N. W. et al. Gate-controlled quantum dots and superconductivity in planar germanium. *Nat. Commun.* **9**, 2835 (2018).
- Watzinger, H. et al. A germanium hole spin qubit. *Nat. Commun.* **9**, 3902 (2018).
- Hendrickx, N. W. et al. A single-hole spin qubit. *Nat. Commun.* **11**, 3478 (2020).
- Lodari, M. et al. Low percolation density and charge noise with holes in germanium. *Mater. Quantum Technol.* **1**, 011002 (2021).
- Jirovec, D. et al. A singlet-triplet hole spin qubit in planar Ge. *Nat. Mater.* **20**, 1106–1112 (2021).
- Hendrickx, N. W., Franke, D. P., Sammak, A., Scappucci, G. & Veldhorst, M. Fast two-qubit logic with holes in germanium. *Nature* **577**, 487–491 (2020).
- Hendrickx, N. W. et al. A four-qubit germanium quantum processor. *Nature* **591**, 580–585 (2021).
- Pauling, L. The nature of chemical bonds. Application of results obtained from quantum mechanics and from a theory of paramagnetic susceptibility to the structures of molecules. *J. Am. Chem. Soc.* **53**, 1367–1400 (1931).
- Anderson, P. W. The resonating valence bond state in La_2CuO_4 and superconductivity. *Science* **235**, 1196–1198 (1987).
- Kivelson, S. A., Rokhsar, D. S. & Sethna, J. P. Topology of the resonating valence-bond state: Solitons and high- T_c superconductivity. *Phys. Rev. B* **35**, 8865–8868 (1987).
- Diep, H. T. (ed.) *Frustrated Spin Systems* 2nd edn (World Scientific Publishing, 2013).
- Zhou, Y., Kanoda, K. & Ng, T.-K. Quantum spin liquid states. *Rev. Mod. Phys.* **89**, 025003 (2017).
- Trebst, S., Schollwöck, U., Troyer, M. & Zoller, P. d -wave resonating valence bond states of fermionic atoms in optical lattices. *Phys. Rev. Lett.* **96**, 250402 (2006).
- Nascimbène, S. et al. Experimental realization of plaquette resonating valence-bond states with ultracold atoms in optical superlattices. *Phys. Rev. Lett.* **108**, 205301 (2012).
- Ma, X.-S., Dakic, B., Naylor, W., Zeilinger, A. & Walther, W. Quantum simulation of the wavefunction to probe frustrated Heisenberg spin systems. *Nat. Phys.* **7**, 399–405 (2011).
- Yang, K. et al. Probing resonating valence bond states in artificial quantum magnets. *Nat. Commun.* **12**, 993 (2021).
- van Riggelen, F. et al. A two-dimensional array of single-hole quantum dots. *Appl. Phys. Lett.* **118**, 044002 (2021).
- Petta, J. R. et al. Coherent manipulation of coupled electron spins in semiconductor quantum dots. *Science* **309**, 2180–2184 (2005).
- Petta, J. R., Lu, H. & Gossard, A. C. A coherent beam splitter for electronic spin states. *Science* **327**, 669–672 (2010).
- Wu, X. et al. Two-axis control of a singlet-triplet qubit with an integrated micromagnet. *PNAS* **111**, 11938–11942 (2014).
- Jirovec, D. et al. Dynamics of hole singlet-triplet qubits with large g -factor differences. *Phys. Rev. Lett.* **128**, 126803 (2022).
- Ono, K., Austing, D. G., Tokura, Y. & Tarucha, S. Current rectification by Pauli exclusion in a weakly coupled double quantum dot system. *Science* **297**, 1313–1317 (2002).
- Studenikin, S. A. et al. Enhanced charge detection of spin qubit readout via an intermediate state. *Appl. Phys. Lett.* **101**, 233101 (2012).
- Harvey-Collard, P. et al. High-fidelity single-shot readout for a spin qubit via an enhanced latching mechanism. *Phys. Rev. X* **8**, 021046 (2018).
- Shulman, M. D. et al. Demonstration of entanglement of electrostatically coupled singlet-triplet qubits. *Science* **336**, 202–205 (2012).
- Piot, N. et al. A single hole spin with enhanced coherence in natural silicon. *Nat. Nanotechnol.* **17**, 1072–1077 (2022).
- Levy, J. Universal quantum computation with spin-1/2 pairs and Heisenberg exchange. *Phys. Rev. Lett.* **89**, 147902 (2002).
- Li, R., Hu, X. & You, J. Q. Controllable exchange coupling between two singlet-triplet qubits. *Phys. Rev. B* **86**, 205306 (2012).
- Klinovaja, J., Stepanenko, D., Halperin, B. I. & Loss, D. Exchange-based CNOT gates for singlet-triplet qubits with spin-orbit interaction. *Phys. Rev. B* **86**, 085423 (2012).
- Wardrop, M. P. & Doherty, A. C. Exchange-based two-qubit gate for singlet-triplet qubits. *Phys. Rev. B* **90**, 045418 (2014).
- Lidar, D. A., Chuang, I. L. & Whaley, K. B. Decoherence-free subspaces for quantum computation. *Phys. Rev. Lett.* **81**, 2594–2597 (1998).

ACKNOWLEDGEMENTS

We thank T.-K. Hsiao, M. Rimbach-Russ, L.M.K. Vandersypen for their valuable advices and feedback. We also thank the other members of the Veldhorst and Vandersypen groups for stimulating discussions. We acknowledge O. Benningshof and R. Schouten for their technical support, and S.G.J. Philips and S.L. de Snoo for their help on software development. We acknowledge support through an ERC Starting Grant and through an NWO projectruimte. Research was sponsored by the Army Research Office (ARO) and was accomplished under Grant No. W911NF-17-1-0274. The views and conclusions contained in this document are those of the authors and should not be interpreted as representing the official policies, either expressed or implied, of the Army Research Office (ARO), or the U.S. Government. The U.S. Government is authorized to reproduce and distribute reprints for Government purposes notwithstanding any copyright notation herein. This publication is part of the 'Quantum Inspire—the Dutch Quantum Computer in the Cloud' project (with project number [NWA.1292.19.194]) of the NWA research program 'Research on Routes by Consortia (ORC)', which is funded by the Netherlands Organization for Scientific Research (NWO).

AUTHOR CONTRIBUTIONS

C.-A.W., C.D. and H.T. performed the experiments. C.-A.W. and C.D. analyzed the data with inputs from all authors. C.-A.W. performed the numerical simulations. C.D. and M.V. wrote the paper with the inputs of all coauthors. W.I.L.L. fabricated the device with inputs from N.W.H. A.S. and G.S. provided the heterostructure. M.V. supervised the project.

COMPETING INTERESTS

The authors declare no competing interests.

ADDITIONAL INFORMATION

Supplementary information The online version contains supplementary material available at <https://doi.org/10.1038/s41534-023-00727-3>.

Correspondence and requests for materials should be addressed to Menno Veldhorst.

Reprints and permission information is available at <http://www.nature.com/reprints>

Publisher's note Springer Nature remains neutral with regard to jurisdictional claims in published maps and institutional affiliations.



Open Access This article is licensed under a Creative Commons Attribution 4.0 International License, which permits use, sharing, adaptation, distribution and reproduction in any medium or format, as long as you give appropriate credit to the original author(s) and the source, provide a link to the Creative Commons license, and indicate if changes were made. The images or other third party material in this article are included in the article's Creative Commons license, unless indicated otherwise in a credit line to the material. If material is not included in the article's Creative Commons license and your intended use is not permitted by statutory regulation or exceeds the permitted use, you will need to obtain permission directly from the copyright holder. To view a copy of this license, visit <http://creativecommons.org/licenses/by/4.0/>.

© The Author(s) 2023